

The Number of Magnetic Null Points in the Quiet Sun Corona

D.W. Longcope,¹ C.E. Parnell²

1. *Department of Physics, Montana State University
Bozeman, Montana 59717*

2. *School of Mathematics and Statistics, University of St Andrews,
St Andrews, Fife, UK, KY16 9SS*

Draft: February 11, 2022

ABSTRACT

The coronal magnetic field above a particular photospheric region will vanish at a certain number of points, called null points. These points can be found directly in a potential field extrapolation or their density can be estimated from Fourier spectrum of the magnetogram. The spectral estimate, which assumes that the extrapolated field is random, homogeneous and has Gaussian statistics, is found here to be relatively accurate for quiet Sun magnetograms from SOHO's MDI. The majority of null points occur at low altitudes, and their distribution is dictated by high wavenumbers in the Fourier spectrum. This portion of the spectrum is affected by Poisson noise, and as many as five-sixths of null points identified from a direct extrapolation can be attributed to noise. The null distribution above 1500 km is found to depend on wavelengths that are reliably measured by MDI in either its low-resolution or high-resolution mode. After correcting the spectrum to remove white noise and compensate for the modulation transfer function we find that a potential field extrapolation contains, on average, one magnetic null point, with altitude greater than 1.5 Mm, above every 322 Mm² patch of quiet Sun. Analysis of 562 quiet Sun magnetograms spanning the two latest solar minima shows that the null point density is relatively constant with roughly 10% day-to-day variation. At heights above 1.5 Mm, the null point density decreases approximately as the inverse cube of height. The photospheric field in the quiet Sun is well approximated as that from discrete elements with mean flux $\langle |\phi| \rangle = 1.0 \times 10^{19}$ Mx distributed randomly with density $n = 0.007$ Mm⁻².

Subject headings: MHD — Sun: corona — Sun: magnetic fields

1. Introduction

Models of magnetic reconnection, from the very earliest, have assigned particular significance to points where the magnetic field vanishes: magnetic null points (Dungey 1958; Sweet 1958). In two-dimensional reconnection models, null points (also called neutral points) are natural locations to change magnetic field line topology. While three dimensions offer alternatives for topological change (Greene 1988; Hesse and Schindler 1988), null points are still natural locations for current intensification (Craig, Fabling and Henton 1995; Rickard and Titov 1996; Galsgaard and Nordlund 1997; Pontin and Galsgaard 2007) and for focusing of magnetosonic waves (Hassam 1992; Craig and McClymont 1993; McLaughlin and Hood 2004). Dissipation of magnetic energy at magnetic null points is therefore a potential source of heat in the quiet Sun corona. The effectiveness of this dissipation for heating the entire corona will depend, in part, in how null points are distributed throughout its field.

Coronal jets are taken as another observational manifestation of coronal null points. Observations in EUV and X-rays show that jets, with their characteristic apex cusp (Shibata *et al.* 1992; Shimojo *et al.* 1996), appear to be more common in coronal holes and the quiet Sun than previously believed (Culhane *et al.* 2007; Cirtain *et al.* 2007). Theoretical models of jets invoke magnetic reconnection occurring at a null point many megameters above the photospheric surface (Yokoyama and Shibata 1996; Moreno-Insertis, Galsgaard and Ugarte-Urra 2008). In order that such a model apply to the large number of jets observed it would be necessary that magnetic null points are relatively common at the altitudes of observed cusps.

In many models, coronal null points occur above a photospheric field consisting of one magnetic element completely surrounded by a ring of opposing polarity (Antiochos 1998; Moreno-Insertis, Galsgaard and Ugarte-Urra 2008). The null point will persist even if the continuous surrounding ring is broken, but it remains necessary that opposing polarity be found on “all sides” of the central element (Seehafer 1986; Beveridge, Priest and Brown 2004). This suggests that coronal null points occur only under special circumstances which are likely to be found infrequently in the actual solar photosphere, and raises once more the question of how common null points might be in the actual coronal magnetic field.

One recent investigation by Régnier, Parnell and Haynes (2008) found 80 magnetic null points over a $102 \text{ Mm} \times 116 \text{ Mm}$ patch of quiet Sun. A potential field was extrapolated onto a rectilinear grid from a magnetogram made by Hinode’s NFI instrument. The algorithm of Haynes and Parnell (2007) was then applied to the gridded field to locate all points where an interpolated field would vanish. This revealed that, at least over that region at that time, there was a column of $N_n = 6.7 \times 10^{-3}$ null points per square megameter, about half above a height of $z = 1 \text{ Mm}$. Close, Parnell and Priest (2004) extrapolating from high-resolution MDI magnetograms of a different day found $1.7 \times 10^{-3} \text{ Mm}^{-2}$, almost four times fewer. This

discrepancy suggests a potential dependence on instrument and specific date of observation. A more general measurement of null point density, applicable to any time or any region, would require the repetition of this process.

Several investigations have estimated the density of magnetic null points in generic quiet Sun coronal fields. Schrijver and Title (2002) modeled the photospheric field of the quiet Sun as a balanced, random distribution of magnetic point charges. They found that the potential field anchored to these charges vanished at one point in the corona, on average, for every eleven point charges on the photosphere. They estimated that the density of null points diminished exponentially with height.

Longcope, Brown and Priest (2003, hereafter LBP03) developed a more general approach to estimating the density of coronal null points in a potential coronal field. They assumed the corona had a random, Gaussian magnetic field, anchored to a statistically homogeneous photospheric field with a known power spectrum $S(k)$. The density of null points at a given height, $\rho_N(z)$, scaled with the inverse cube of the characteristic scale length at that height. This was expressed in terms of integrals of the power spectrum, $S(k)$, as well as on the mean of the vertical field, \bar{B}_z . At lower heights it depended on larger wave numbers (smaller scales). A perfectly flat spectrum, such as from ideal white noise or a distribution of point magnetic charges, introduces no length scale of its own. In this case the density decreases with height as

$$\rho_N(z) = \frac{0.040}{z^3} , \quad (1)$$

independent of the strength or other properties of the photospheric field.

The spectrum from a magnetogram can be used in the spectral estimate of LBP03 to compute the distribution of nulls above observed regions. Its assumption of randomness and homogeneity are likely to be fairly valid in quiet Sun regions. In this work we quantify the degree to which a potential field extrapolation satisfies the other assumption, that the field components are Gaussian random variables. We also test the estimate against the distribution of null points found directly in an extrapolated field. We find evidence that the spectral estimate gives a reasonable approximation of the number of magnetic null points above a region of quiet Sun, especially above 1,500 km from the magnetogram surface.

The spectra of MDI magnetograms reveal several factors which could affect the number of null points found either directly or through spectral estimate. There is a level of white noise which, while reduced by averaging, is present in any magnetogram. We find that removing its contribution from a spectrum reduces the number of null points by as much as 85%. The defocusing of the telescope, partly on purpose in the low-resolution mode, steepens the spectrum, causing an underestimation of the number of null points. Both of these effects

can be removed from the power spectrum, $S(k)$, yielding a spectral estimate of null points less affected by instrumental artifacts.

We perform spectral estimates on 562 MDI magnetograms of quiet Sun during the two solar minima it has observed (1996–1998 and 2006–2007). After compensating for the effects mentioned above, we find the number of coronal null points above 1.5 Mm to be fairly constant: $N_n = 3.1 \times 10^{-3} \pm 3.0 \times 10^{-4} \text{ Mm}^{-2}$. That is, on average, one such null point over every 322 Mm^2 patch of quiet Sun. When the Sun is completely free of active regions this amounts to about 20,000 null points above the solar surface.

The magnetic spectrum of the quiet Sun is found to be remarkably consistent over the periods investigated. The typical spectrum is consistent with a potential field from magnetic point sources located about 1.4 Mm *below* the photospheric surface. The variance and kurtosis of the magnetograms can be used to infer the size and areal density of these sources. Assuming them to have an exponential distribution of fluxes we find the sources have mean flux, $\langle |\phi| \rangle = 1.0 \times 10^{19} \text{ Mx}$ and areal density $n = 0.007 \text{ Mm}^{-2}$.

The paper is structured as follows. In the next section we assess the degree to which potential fields, extrapolated from two particular MDI magnetograms, satisfy the assumptions of the LBP03 spectral estimate. We then directly locate all of the null points in extrapolations from these magnetograms and compare the results to the spectral estimate. In §3 we apply the spectral estimate to 562 MDI magnetograms spanning solar minimum periods in 1996–1998 and 2006–2007. We find that the number of coronal null points stays at a relatively constant level, with $\sim 10\%$ day-to-day variation. In §4 we show how the generic spectrum of the quiet Sun photosphere may be interpreted as a random super-position of identical magnetic elements. We infer the properties of the elements and their distribution from the Fourier spectrum. Once again, these properties appear relatively constant over time. Finally, we discuss what our findings imply about null points in the actual coronal field above quiet Sun.

2. Distribution of Nulls

2.1. The Gaussianity of the extrapolated field

The basis for our computation will be magnetograms from regions of quiet Sun, near disk center. Figure 1 shows two examples of such magnetograms, each made by averaging five one-minute cadence MDI line-of-sight magnetograms. The field of view is $300'' \times 300''$ centered at disk center. The left and right images are from high-resolution and low-resolution data obtained 1.75 hours apart.

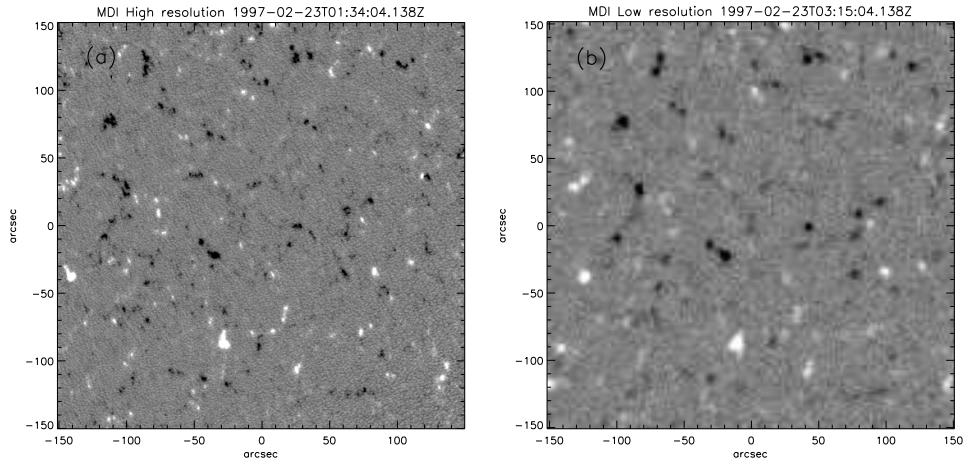


Fig. 1.— Magnetograms of a quiet sun area from 23 Feb. 1997, made by averaging five consecutive MDI magnetograms made at one-minute cadence. The grey scale shows the line of sight field between ± 100 Gauss. (a) High resolution magnetograms and (b) Low resolution magnetograms from 1:45 later.

The spectral estimate of LBP03 yields the spatial density of null points in a coronal magnetic field satisfying certain conditions. It assumes the coronal field to be potential and to be anchored to a random photospheric field whose statistics are homogeneous and Gaussian. These conditions on the photospheric field (the magnetogram) lead to a coronal field whose components are statistically homogeneous and Gaussian. From the properties of this field LBP03 reports the mean density of null points at any height in the corona.

Extrapolating upward from the magnetogram of Figure 1a to a particular height z results in a new field, $B_z(x, y, z)$, whose histogram we find to be nearly Gaussian. Figure 2 shows histograms from several heights as solid lines, and the Gaussians best fitting their central portions as dashed curves. The cumulative distribution from a range of values was fitted, and the range was iteratively adjusted until it contained exactly two standard deviations to either side. The standard deviation of this fit, $\sigma_z^{(g)}$, is indicated by triangles and plotted on axes to the left. The standard deviation of the entire field, $\sigma_z^{(m)}$, plotted with a dashed line on the same axis is systematically greater than that of the core.

It can be seen in Figure 2, that the field B_z has an approximately Gaussian distribution even well above the photospheric level ($z = 0$). At the bottom, the Gaussian component has a standard deviation, $\sigma_z^{(g)} \simeq 11.3$ Gauss, comparable to the intrinsic noise in a five-minute average of MDI magnetograms (Liu and Norton 2001); it decreases with height as the width of the Gaussian narrows. The actual distribution departs from the Gaussian fit principally by an excess (tail) mostly outside $\pm \sigma_z^{(g)}$. Histograms made from the horizontal components

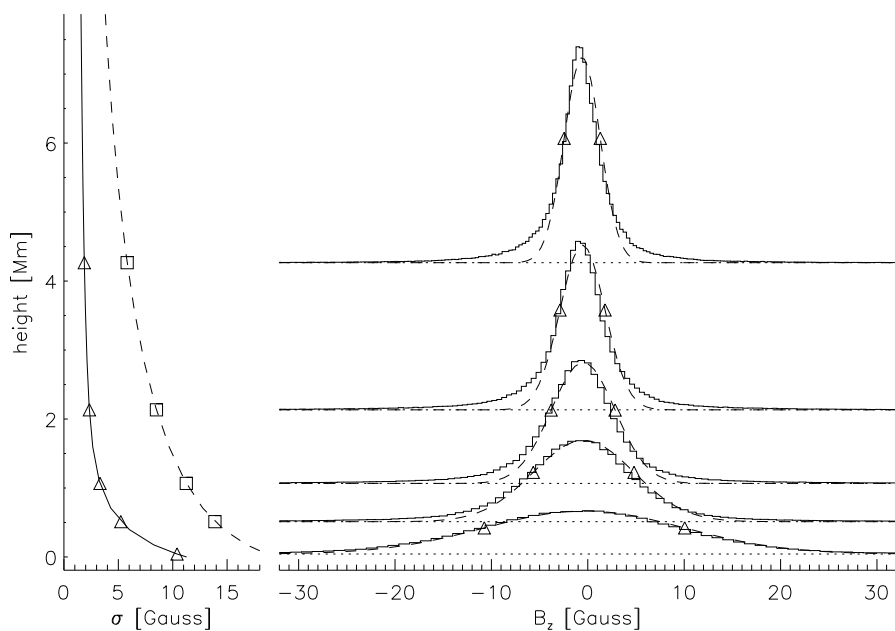


Fig. 2.— Histograms of the field B_z computed by extrapolating the photospheric magnetograms to five different heights. The height, in Mm, of the slice corresponds to the level of the bottom of the histogram on the far left axis. A Gaussian fit to the central region is shown as a dashed line, with triangles at $\pm\sigma_z^{(g)}$. These values are also plotted against a horizontal axis on the left. A solid curve shows the full functional form of $\sigma_z^{(g)}(z)$. A dashed line shows $\sigma_z^{(m)}(z)$ on the same axis (squares occur at heights coincident with the histograms).

of the extrapolated fields at varying heights look very similar to those of the vertical field shown in Figure 2.

The Gaussian fit to the central core of each distribution can be used to quantify the degree to which the actual field is a Gaussian variable. The amplitude of the Gaussian component ranges from 0.97 at $z = 0$ to 0.81 higher up (see Figure 3b). That is to say the field is between 81% and 97% Gaussian.

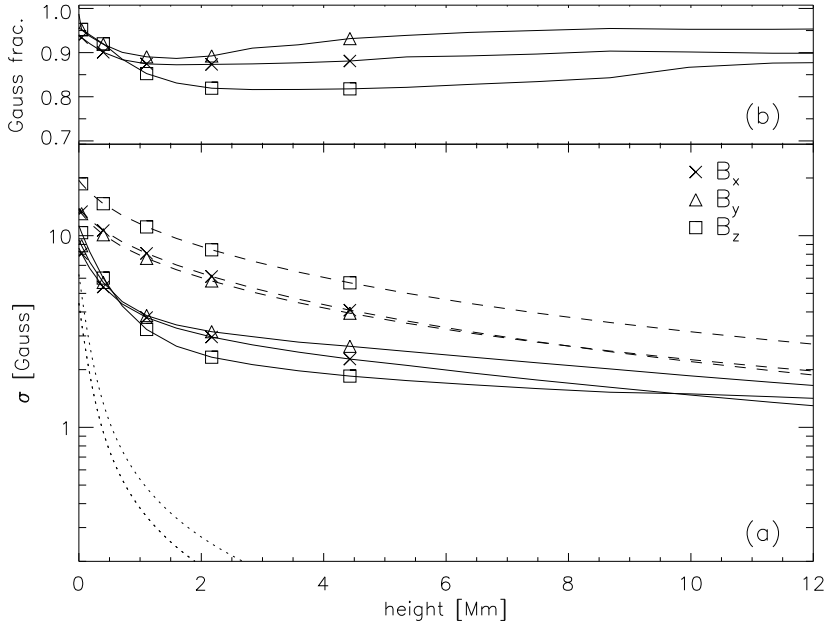


Fig. 3.— (a) Standard deviations from all three components of the potential extrapolation of the magnetogram Figure 1a. The solid and dashed curves show $\sigma^{(g)}$ and $\sigma^{(m)}$ respectively for B_x (crosses), B_y (triangles) and B_z (squares), plotted versus height. The symbols occur at the same heights as the histograms from Figure 2. Dotted lines show the standard deviation for vertical (upper) and horizontal (lower) field components extrapolated from white noise. (b) The fraction of each field which is fitted by the Gaussian within the central $4\sigma^{(g)}$.

While a significant component of the magnetic field has a Gaussian distribution, it is not spatial white noise. Longcope, Brown and Priest (LBP03) show that a potential field extrapolated from a magnetogram with isotropic power spectral density (psd) $S(k)$ has vertical field with variance

$$\sigma_z^2(z) = 2\pi \int_0^\infty S(k) e^{-2kz} k dk = 2\sigma_x^2(z) = 2\sigma_y^2(z) . \quad (2)$$

Spatial white noise is uncorrelated from pixel to pixel and therefore has a flat psd

$$S(k) \simeq \frac{\sigma_0^2}{\pi k_c^2} \Theta(k_c - k) \quad , \quad (3)$$

out to the resolution limit $k_c = 2\sqrt{\pi}/\Delta x$ for pixel size Δx (Θ is the Heaviside function). Using this in (2) gives the variance due to spatial white noise alone

$$\sigma_z^2(z) = \frac{\sigma_0^2}{8\pi(z/\Delta x)^2} \left[1 - (1 + 4\sqrt{\pi}z/\Delta x)e^{-4\sqrt{\pi}z/\Delta x} \right] \quad . \quad (4)$$

This functional form, plotted as a dotted line for each component of the field in Figure 3, falls off much faster than either $\sigma^{(g)}$ or $\sigma^{(m)}$. We therefore conclude that the Gaussian component consists of contributions with spatial correlations longer than a single pixel: it is not white noise.

It is common practice to assess the degree to which a variable departs from Gaussian by its kurtosis statistic, K . The kurtosis is the fourth moment divided by the square of the variance, less three; when the variable is perfectly Gaussian $K = 0$. Excesses, relative to a Gaussian, in the tails of the distribution will elevate the fourth moment and lead to a positive kurtosis. Figure 4 shows that even when the excess tails account for 3% of the distribution, they lead to a large kurtosis.

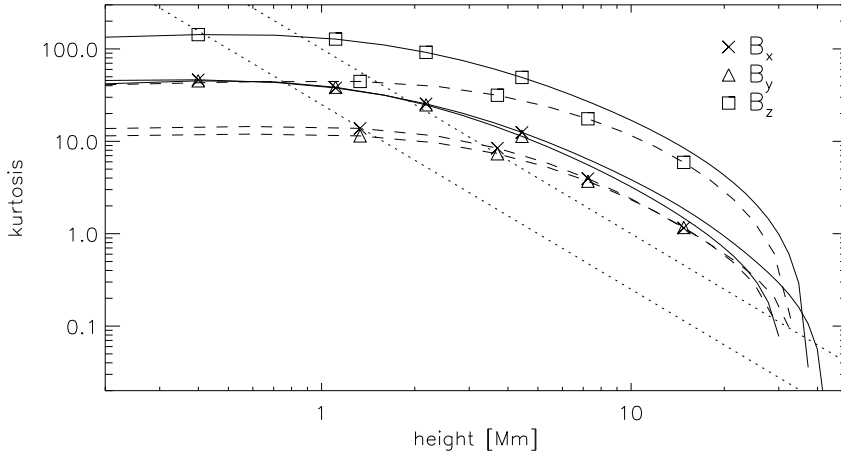


Fig. 4.— The kurtosis of the fields for B_x (crosses), B_y (triangles) and B_z (squares), plotted versus height. Solid and dashed lines are for the high resolution and low resolution magnetograms respectively. The dotted lines show the results for point magnetic sources, taken from Equation (6).

For comparison, a distribution of n point sources per unit surface area has a flat power

spectrum with no cut-off ($k_c \rightarrow \infty$) whose variance is (LBP03)

$$\sigma_z^2(z) = \frac{n\langle\phi^2\rangle}{8\pi z^2} , \quad (5)$$

where $\langle\phi^2\rangle$ is the variance in the source fluxes. The kurtosis of this same photospheric field is

$$K_z = \frac{4}{5\pi} \frac{\langle\phi^4\rangle}{\langle\phi^2\rangle^2} \frac{1}{nz^2} = 4K_x = 4K_y . \quad (6)$$

Both of the expressions above diverge at the photosphere ($z \rightarrow 0$) as a consequence of the very strong fields in the neighborhood of a point source. This divergence is one element leading to the failure of the spectral estimate at low heights, $z < n^{-1/2}$ (LBP03).

It is evident from Figure 4 that the kurtosis of the actual field is generally large but remains finite even as $z \rightarrow 0$. The large magnitude arises from the tails in the pdf corresponding to those pixels of the magnetogram in magnetic elements, where $|B_z| > 5\sigma_z(0) \simeq 50$ Gauss. These are the excess tails of the distribution function, but they are also the structures which generate field above a few megameters.

2.2. Assessing the accuracy of the spectral estimate

A spectral estimate of the magnetic null point density is found from the isotropic power spectrum, $S(k)$, of the photospheric magnetogram. The spectrum determines the variance, as given by Equation (2), and a related quantity

$$q^2(z) = \frac{2\pi}{\sigma_z^2(z)} \int_0^\infty S(k) e^{-2kz} k^3 dk . \quad (7)$$

Provided the field has Gaussian statistics the density of null points in it is found to be

$$\rho_N(z) = G(\bar{B}_z/\sigma_z) q^3(z) , \quad (8)$$

where $G(\zeta)$ is a dimensionless function defined in LBP03. The function depends on the mean vertical field strength \bar{B}_z and also weakly on another moment of the spectrum. Provided the polarities are sufficiently balanced that $\bar{B}_z \ll \sigma_z$ over the relevant range of heights, we find $G \sim 2 \times 10^{-2}$ for most spectra of quiet Sun magnetograms.

We assess the accuracy of the approximation offered by the spectral estimate by direct comparison. Both magnetograms from Figure 1 are extrapolated onto a rectilinear grid with periodic lateral boundaries. Between the grid points the magnetic field is defined using tri-linear interpolation. A magnetic null point is the point where all three components of

this interpolated field vanish together. These null points are located using the algorithm of Haynes and Parnell (2007). The number of null points found above a given height z is divided by the photospheric area to yield a null-point column density, $N_n(z)$. The right and left axes of Figure 5b shows the number and column densities found this way, respectively.

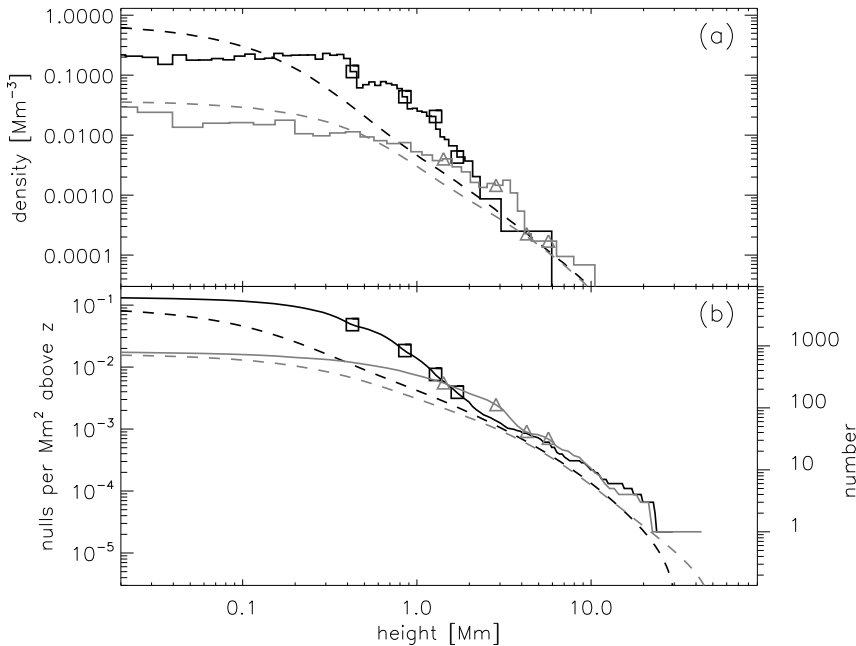


Fig. 5.— The density (a) and column density (b) of null points in potential fields extrapolated from the MDI magnetograms in Figure 1. Dark and light curves correspond to the high resolution and low resolution data respectively. The solid curves are computed by finding the nulls on a gridded extrapolation; the dashed curves are the spectral estimates. Symbols appear at heights of one, two, three and four horizontal pixel sizes ($z = \Delta x, 2\Delta x, 3\Delta x$ and $4\Delta x$). For panel (b) the left axis reports the column density in nulls per Mm^2 above a given height, while the right axis gives the total number over the entire magnetogram.

There are more null points in the high resolution case (dark curves) than in the low resolution (6135 *vs.* 664). The majority of the excess null points lie in a layer about one Mm thick. Over heights above one Mm the predicted null columns (dashed curves on Figure 5b) from the high resolution and low resolution cases are quite similar. The greatest disagreement between the actual null column, $N_n(z)$, and the spectral estimate occurs within this same one Mm bottom layer. Above this height the two estimates are within a factor of two of reality for both resolutions. Since the bottom layer of the high resolution field has the largest kurtosis it is perhaps unsurprising that the greatest disagreement with the spectral estimate

occurs there. Perhaps more surprising is that kurtosis as large as 40 (the maximum of the low resolution data) leads to disagreement by not more than a factor of two.

3. The quiet Sun null column in general

3.1. Comparing nulls from different magnetograms

The extent to which, for levels above one Mm, the spectral estimates of high resolution and low resolution agree can be understood from a comparison of their power spectra $S(k)$, as shown in Figure 6. A fast Fourier transform (FFT) of the $L_x \times L_y$ magnetogram returns an array of complex coefficients, $\hat{B}_{m,n}$, for the expansion

$$B_z(x, y) = \sum_{m,n} \hat{B}_{m,n} \exp[i m \Delta k_x x + i n \Delta k_y y] \quad , \quad (9)$$

where $\Delta k_x = 2\pi/L_x$ and $\Delta k_y = 2\pi/L_y$. The quiet-Sun magnetograms have very few features at their edges which might suffer discontinuity under periodic repetition so we find it unnecessary to employ any windowing function (Press *et al.* 1986).

The two-dimensional power spectrum at wave number $\mathbf{k} = m\Delta k_x \hat{\mathbf{x}} + n\Delta k_y \hat{\mathbf{y}}$ is

$$S(\mathbf{k}) = \frac{|\hat{B}_{m,n}|^2}{\Delta k_x \Delta k_y} \quad . \quad (10)$$

This function is defined only on points of the Fourier-space grid, but approximates a continuous function. The denominator in Equation (10) eliminates from $S(\mathbf{k})$ any dependence on pixel size or field of view.

The isotropized power spectrum, $S(k)$, is computed by averaging all values of $S(\mathbf{k})$ within an annulus of Fourier-space. We use annuli of radii extending to a maximum wave number $k_c = 2\sqrt{\pi}/\Delta x$, chosen so that the total Fourier-space area, πk_c^2 , matches that occupied by the actual magnetogram. The cut-offs for high and low resolution MDI magnetograms are therefore 8.2 rad/Mm and 2.5 rad/Mm respectively since these have pixel sizes of $\Delta x = 0.43$ Mm and $\Delta x = 1.42$ Mm in this particular magnetogram.

The spectrum in Equation (10) is normalized so that,

$$\langle B_z^2 \rangle = \sum_{m,n} |\hat{B}_{m,n}|^2 \simeq \int S(\mathbf{k}) d^2k = 2\pi \int_0^{k_c} S(k) k dk \quad ,$$

where the angled brackets are a spatial average. The variance is found from the same expression but excluding from the sum $(m, n) = (0, 0)$. The variance at height z above the

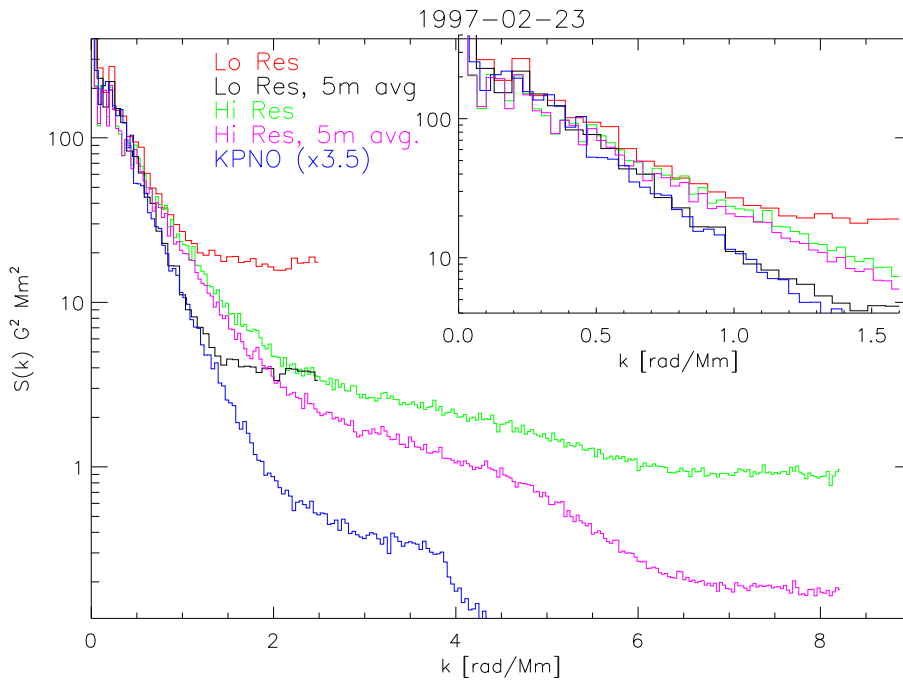


Fig. 6.— The isotropized spectra for $300'' \times 300''$ magnetograms of quiet Sun centered at disk center on 23 Feb. 1997. Curves of different colors are $S(k)$ for 30-second MDI exposures at high (green) and low (red) resolution; 5-minute averages at high (magenta) and low (black) resolution; and Kitt Peak magnetogram (blue). The inset is an expansion of the region at low wavenumbers.

magnetogram plane, Equation (2), includes an exponential factor from the potential field extrapolation.

Each spectra from an MDI magnetogram in Figure 6 has a range of white noise over its highest wave numbers. We estimate its level, S_n , from the median value of $S(k)$ over the highest 15 spectral bins. The noise level is reduced by exactly 1/5 in the averages strongly suggesting an origin in Poisson counting noise, uncorrelated between frames (Liu and Norton 2001; DeForest *et al.* 2007). The flat noise floors contribute $\sigma_z^2(0) = \pi k_c S_n^2 = (8.8 \text{ G})^2$ and $(6.3 \text{ G})^2$ to the low and high-resolution variances respectively. We noise-correct each spectrum by subtracting from the entire curve the flat noise floor, S_n , determined from the top 15 spectral bins.

Each of the noise-corrected spectra appears to have been steepened by the modulation transfer function (MTF), $M(k)$, of its imaging system (Born and Wolf 1980), and must be corrected to $S(k)/M^2(k)$. The most conservative correction to the high-resolution spectrum is to assume it to be diffraction-limited and take $M(k) = M_d(k)$, given in an appendix. MDI is intentionally defocussed in its low-resolution mode, leading to an MTF we approximate as $M^2(k) = M_d^2(k)/(1 + \ell_0^4 k^4)$ where $\ell_0 \simeq 1.6''$ at this time (see appendix). Performing these corrections restores all four MDI spectra to similar forms, over low wave-numbers, as shown in Figure 7. The Kitt Peak spectrum (blue) remains below all others since it has not been divided by its MTF, part of which presumably arises from atmospheric seeing (Hufnagel and Stanley 1964; Abramenko *et al.* 2001).

There is, over the range $k > 1.5 \text{ rad/Mm}$, an excess in high-resolution power, relative to low-resolution; this excess is further amplified by the MTF correction. The excess might be partly an artifact from the granular motions during the brief intervals between different filter-gram exposures (DeForest *et al.* 2007). Its origin, whatever that may be, is evidently correlated several-fold longer than five minutes, since averaging diminishes it by less than a factor of five. We next show that this power does not significantly affect the null densities at heights where potential field extrapolation is warranted.

The spectra from Figure 6 are used in the Laplace transform integrals, (2) and (7), from which are computed the null density $\rho_N(z)$, according to Equation (8). This density is integrated downward from some upper height yielding the null column density, $N_n(z)$, plotted in Figure 8. The exponential factor, e^{-2kz} , in each of the spectral integrals means that the null density at a given height z depends principally on the spectrum over wave numbers $k < 1/z$. Thus heights above $z = 1 \text{ Mm}$ depend mostly on the spectrum below (to the left of) $k = 1 \text{ rad/Mm}$. As discussed above, and evident in Figure 7, all MDI spectra are fairly similar over this range. It is therefore natural that all five solid curves in Figure 8 follow similar paths above one Mm.

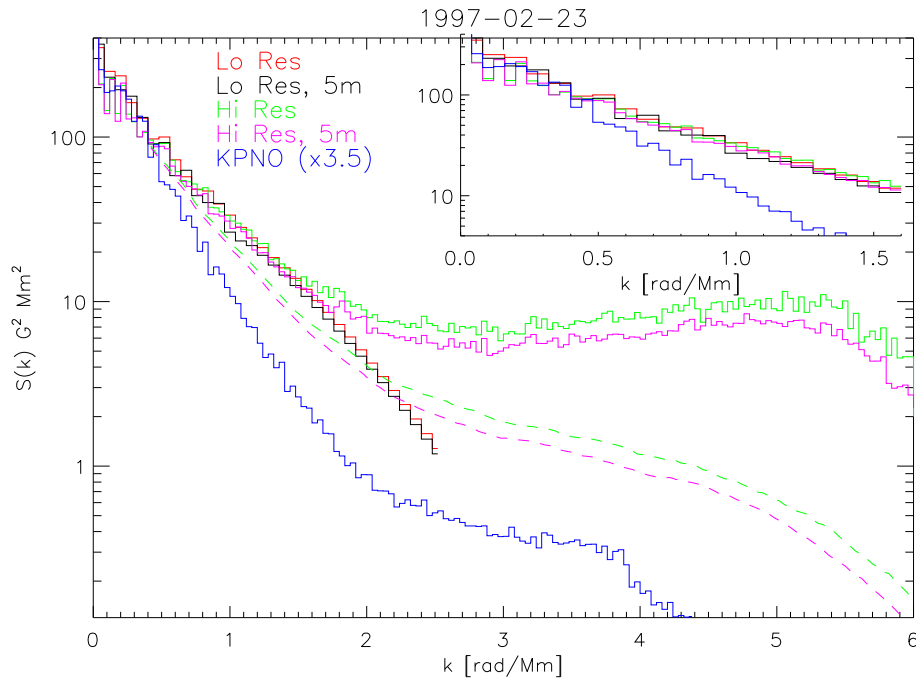


Fig. 7.— The same spectra from Figure 6 after removal of white noise and correction for the MTF. No corrections are performed on the Kitt Peak spectra (blue) which is retained for reference. Dashed curves show the high resolution spectra before it was corrected for the MTF, but after white noise was removed.

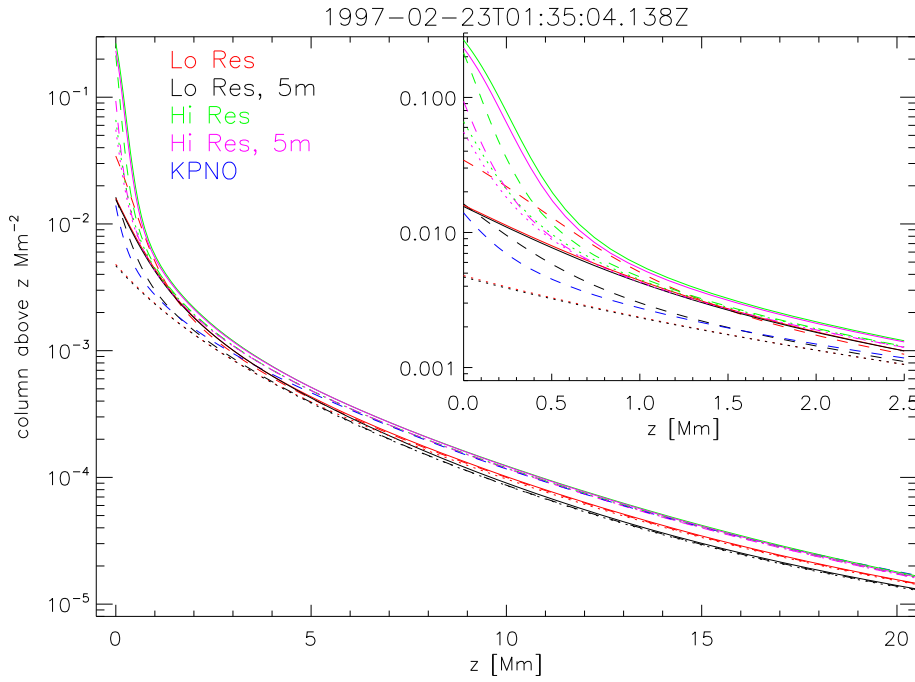


Fig. 8.— Spectral estimates of the null column densities, $N_n(z)$, computed from each of the spectra in Figures 6 and 7 using the same color code. Dashed curves are from the original spectra (Figure 7); solid curves are from spectra from which white noise has been subtracted and which have been divided by the MTF (Figure 7). Dotted lines show the curves after noise subtraction without MTF correction.

Noise contributes significant power to the highest wavenumbers, creating a population of artificial null points in an extrapolation. The null column densities after subtraction of this noise, the dotted curves in Figure 8, lie below the corresponding uncorrected (dashed) curves. The fraction of nulls attributable to noise alone is lower in five-minute averages than one-minute magnetograms, since the former have lower noise. The effect is most pronounced in one-minute low-resolution magnetograms, for which 85% of all nulls are due to noise.

The small-scale structure revealed in high resolution magnetograms translates into complex fields with high null densities at the lowest level of the potential magnetic field. While potential fields are frequently used to approximate the quiet Sun corona, they are of questionable validity in the lowest layers, where the plasma density and pressure are liable to play their most significant role. Above a height of 1,500 km (1.5 Mm) the potential field approximation may be on better footing. It appears from Figure 8 that most of the estimates based on potential field extrapolation, are in reasonable agreement above this particular height (at $z = 1$ Mm, for example, the high and low resolution estimates appear to disagree to a greater extent). For these reasons we hereafter focus on estimating the total column of null points above $z = 1.5$ Mm, denoted $N_n(1.5 \text{ Mm})$.

3.2. The generic behavior

The foregoing sections have considered different magnetograms of the same region of quiet Sun (23 Feb. 1997). In order to generalize our conclusions we perform similar analysis on magnetograms spanning solar minimum from 2006 and 2007. The same central $300'' \times 300''$ sub-image is extracted from one full-disk (low resolution) daily MDI magnetogram every second day. It is analyzed provided there is no obvious active region field, or preponderance of one polarity, and provided there is less than 8×10^{19} Mx in pixels above 200 G. This value was selected after some trial and error to eliminate plage regions whose presence would violate our assumption of homogeneity. Separate analyses are performed for one-minute daily magnetograms and for those composed of 5-minute averages.

The isotropized spectra from all quiet Sun areas turn out to be very similar to one another, closely resembling the example from the previous section. Figure 9 shows a median spectrum: the the median value, at each wave-number, from over 110 quiet Sun spectra of each low-resolution kind. The upper and lower quartile points, bracketing half of all values, are plotted as lighter curves. This clearly shows that the most significant variation occurs at wavenumbers below 0.2 rad/Mm (i.e. wavelengths longer than 30 Mm).

Removing the white noise floor by first subtracting it and then extrapolating the noisier

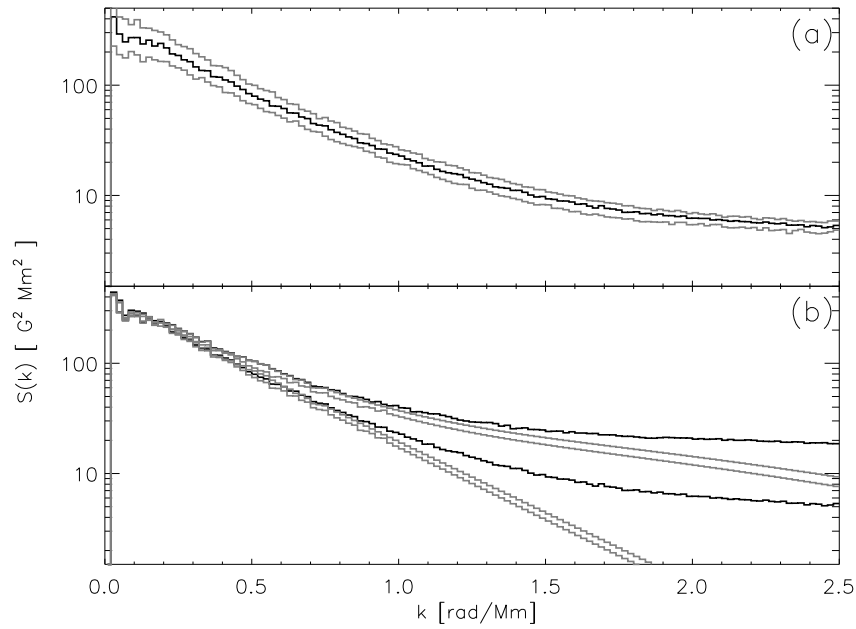


Fig. 9.— Median spectra from magnetograms in 2006 and 2007. (a) The median spectrum (dark) and the upper and lower quartiles (light curves) from the five-minute averages. (b) The median from 118 one-minute magnetograms (upper curve) and 114 5-minute averages (lower curve). The lighter curves show the results of subtracting white noise (lower pair) and then dividing by the MTF (upper pair).

portions yields the lower light spectra in Figure 9b. This is then divided by the empirically determined MTF, $M^2(k) = M_d^2(k)/(1 + \ell_0^4 k^4)$, where $\ell_0 = 1.04''$ as described in the appendix. The results are the two upper light curves.

The column density found from these various versions of the median spectra are shown in Figure 10. The solid curves of each shade are the result of removing noise and correcting for the MTF. The broken curves above these are from the raw spectra, while the dashed curves below are after noise has been removed but no MTF correction performed. Symbols mark the values of these at $z = 1.5$ Mm: $3.0 \times 10^{-3} \text{ Mm}^{-2}$ and $2.9 \times 10^{-3} \text{ Mm}^{-2}$ respectively.

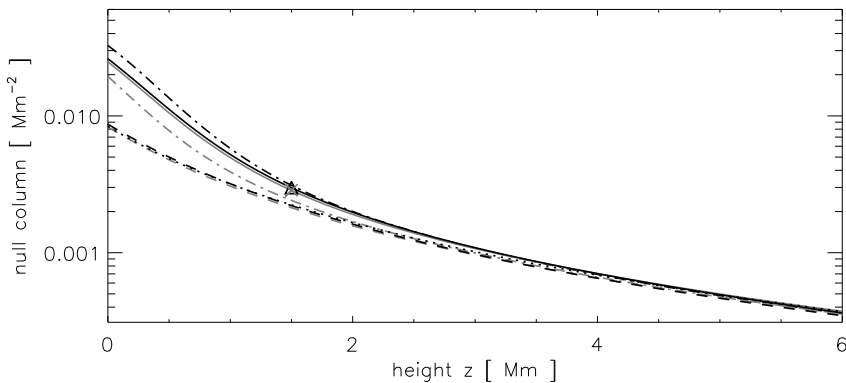


Fig. 10.— The column densities from each of the median spectra in Figure 9b. Dark and light curves are for one-minute magnetograms and five-minute averages respectively. Solid curves are from the entire spectra and dashed curves are from the noise-corrected spectra. A dotted curve is an empirical fit.

The median spectra are clearly very close to pure exponentials, $S(k) \sim e^{-2kd}$. This functional form suggests the empirical model for the null column density of one-minute magnetograms (dotted line)

$$N_n(z) \simeq \frac{0.021}{(z + d)^2} \quad , \quad (11)$$

where the numerator and $d = 1.6$ Mm are found from fitting.

The null column above a given height does vary between magnetograms, as shown in Figure 11. There appear to be random fluctuations superimposed on a much slower variation. We estimated the dispersion about the trend, $2.7 \times 10^{-4} \text{ Mm}^{-2}$ for the one-minute magnetograms and $2.5 \times 10^{-4} \text{ Mm}^{-2}$ for five-minute averages, by subtracting a 90-day running mean. Considering the entire data set of one-minute magnetograms, including its slow trend, we find the column of null points above $z = 1.5 \text{ Mm}$ to be

$$N_n(1.5 \text{ Mm}) = (3.1 \pm 0.3) \times 10^{-3} \text{ Mm}^{-2} .$$

(The errors quoted above represent rms variation; the error in the mean is far smaller.) The value from five-minute magnetograms is slightly lower: $(2.9 \pm 0.3) \times 10^{-3}$. We believe this value is lower partly because of motional blurring during the averaging interval, so we adopt the one-minute-magnetogram value as the more accurate of the two.

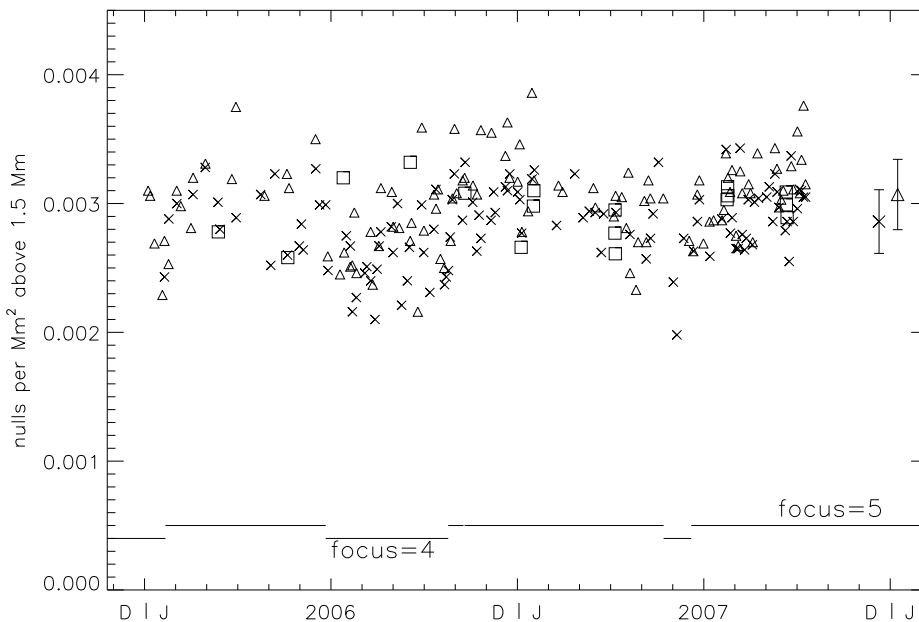


Fig. 11.— The column of null points above $z = 1.5 \text{ Mm}$ found from quiet sun magnetograms spanning 2 years of solar minimum. Triangles and crosses denote one-minute and five-minute low-resolution magnetograms respectively; squares are from high-resolution magnetograms. Error bars on the right show one standard deviation of scatter about a 90-day running mean. Solid lines along the bottom show the reported focus position of the MDI telescope.

We believe the slow variation in $N_n(1.5)$ is due to gradual changes in the MTF of the imaging system. The reported focus position of the instrument is shown as a solid

curve long the bottom. The focus is periodically changed to compensate for changes in the instrument itself. Our estimate of the MTF was performed through cross-comparison to the high resolution images, plotted as squares, all while the instrument was in focus position 5. This is the MTF by which we are correcting the spectrum, so we believe that the value in the middle of this interval is probably the most accurate. The MTF correction raises the low resolution columns by about 40%, thereby making them more consistent with high resolution values. Omitting that step gives null columns which could be considered lower bounds on the actual values: medians are $N_n(1.5) = 2.2 \times 10^{-3} \text{ Mm}^{-2}$ for one-minute and $2.1 \times 10^{-3} \text{ Mm}^{-2}$ for five-minute.

A comparable plot from the previous solar minimum, Figure 12, shows more pronounced evolution on long time scales. This data comes from the very beginning of the SOHO mission, when the instrument was probably changing most rapidly. There is a very large change in Nov. 1997 coincident with the refocussing of the telescope. The later refocussing events in Figure 11 produce much less obvious changes, either because they are more frequent or because there is less dramatic change between them. Due to the larger, and more rapid change we did not attempt an estimate of the MTF. Instead we used the empirical form from the later phase, with $\ell_0 = 1.6''$ found from fitting the 23 Feb. 1997 data described above. This restores the typical values to the same range as they were in the 2006/2007 data set.

4. Modeling the quiet Sun spectrum

4.1. A synthetic magnetogram

Some insight into the origins of the quiet sun magnetic field may be gleaned from its spectrum. Consider a model photospheric field composed of distinct elements, each characterized by the same normalized shape function, $f(\mathbf{x})$. Elements at locations, $\mathbf{x}_j = (x_j, y_j)$, with fluxes, ϕ_j , will create a vertical field

$$B_z(\mathbf{x}) = \sum_j \phi_j f(\mathbf{x} - \mathbf{x}_j) \quad , \quad (12)$$

in the photospheric plane. For simplicity let us assume that the fluxes are random, have zero mean, and are uncorrelated: $\langle \phi_i \phi_j \rangle = \langle \phi^2 \rangle \delta_{ij}$. We also assume that the fluxes are independent of their locations \mathbf{x}_j which are distributed randomly with areal density n . Under these assumptions the power spectrum of the photospheric field is

$$S(\mathbf{k}) = n \langle \phi^2 \rangle |\hat{f}(\mathbf{k})|^2 \quad , \quad (13)$$

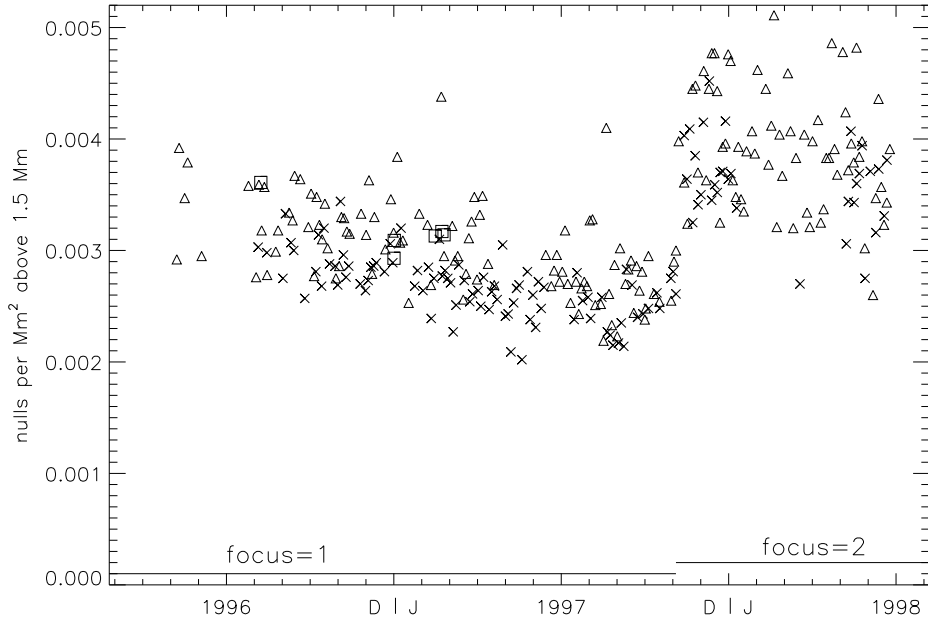


Fig. 12.— Null columns during the solar minimum from 1996-1998. Plot format is the same as in Figure 11.

where $\hat{f}(\mathbf{k})$ is the Fourier transform of the shape function.

A purely exponential spectrum can be interpreted as being composed of individual flux elements each with an exponential Fourier transform such as

$$f(\mathbf{x}) = \frac{1}{2\pi} \frac{d}{(|\mathbf{x}|^2 + d^2)^{3/2}} = \int \frac{e^{-|\mathbf{k}|d}}{(2\pi)^2} e^{i\mathbf{k}\cdot\mathbf{x}} d^2k \quad . \quad (14)$$

This function also happens to be the vertical potential field due to a unit point charge located at $z = -d$; it is the potential field Green's function.

The observed spectrum, before MTF-correction, is very close to an exponential, $S(k) \simeq e^{-2kd}$. The exponent is thus directly related to a “depth” at which point sources are submerged. On the other hand, the spectrum after correction, $S(k) \simeq e^{-2kd}/M^2(k)$, has an inverse Fourier transform which is not a simple function, and does not admit such a suggestive interpretation. Figure 13 shows the functions $f(r)$ for both the uncorrected (dashed) and MTF-corrected (solid) spectra from 23 Feb. 1997. The integrated field (bottom) shows that for each case half of all flux is confined to a similar $r_0 \simeq 4$ Mm circle.

The variance of a photospheric field composed of random elements is

$$\sigma_p^2 = n \langle \phi^2 \rangle \int f^2 d^2x = \frac{n \langle \phi^2 \rangle}{4\pi r_*^2} \quad , \quad (15)$$

where r_* characterizes the radius of the shape function, $f(r)$, through the integral of its square. The parameter is defined to match the root-mean-squared radius of a Gaussian shape. The uncorrected shape function, Equation (14), yields, $r_* = \sqrt{2}d$, whose introduction into Equation (15) returns the variance of the vertical field at a height d above a distribution of point charges, i.e. Equation (5). The MTF-corrected shape function is notably narrower (solid line in Figure 13), under the anticipation that it is broadened by the point spread function to produce the broader observed shape (dashed) with its larger radius r_* .

The kurtosis of the composite field given by expression (12) is

$$K_p = \frac{1}{n} \frac{\langle \phi^4 \rangle}{\langle \phi^2 \rangle^2} \frac{\chi}{4\pi r_*^2} \quad , \quad \chi = (4\pi r_*^2)^3 \int f^4 d^2x \quad , \quad (16)$$

where the dimensionless coefficient χ depends only on the shape of the individual elements, $f(r)$. It is unity for a perfectly flat function and greater as the shape becomes more peaked. For charges submerged at a depth d , the value $\chi = 32/5$ can be inferred by comparison between expressions (6) and (16) and use of the relation $r_* = \sqrt{2}d = \sqrt{2}z$.

The dimensionless ratio, $\xi = \langle \phi^4 \rangle / \langle \phi^2 \rangle^2$, depends only on the distribution of element amplitudes, and not on their size or shape. Flux amplitudes distributed uniformly or exponentially will be characterized by $\xi = 9/5$ or $\xi = 6$ respectively. Parnell (2002) found that

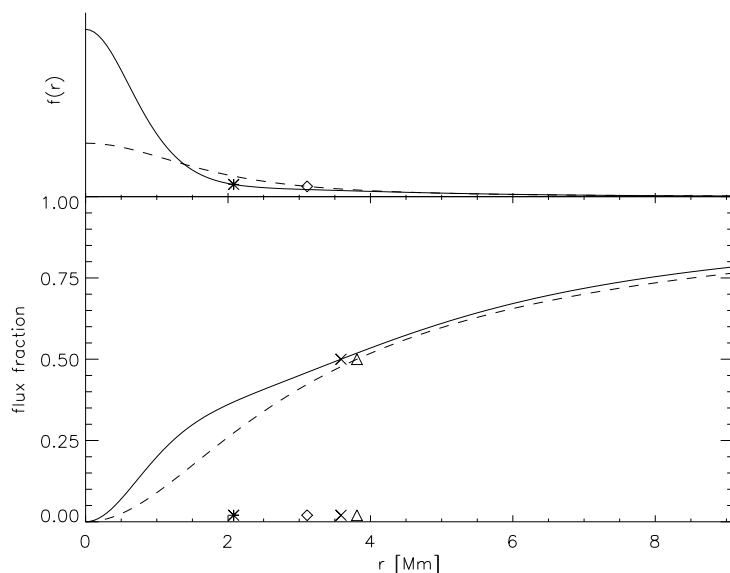


Fig. 13.— The structure of a magnetic element inferred from the power spectrum of a magnetogram. The top curves show the shape functions, $f(r)$, from Equation (14), for an uncorrected exponential spectrum with $d = 2.2$ Mm (dashed) and for the shape after correction for the low-resolution MTF with $\ell_0 = 1.6''$ (solid). Symbols on each curve mark r_* . The vertical scale is the same for each curve and makes $2\pi \int f(r) r dr = 1$. The bottom panel shows the total fraction of flux with a given radius, and symbols mark the radius of half flux.

fluxes of each polarity were distributed with a hybrid between an exponential and power-law known as a Weibull distribution. The particular Weibull distributions reported are characterized by values of ξ between 22 and 30. These are larger than for purely exponential distribution since broader wings lead to more common occurrence of large fluxes.

The variance of Gaussian white noise, σ_n^2 , adds to expression (15) to give the total variance in a magnetogram, $\sigma_0^2 = \sigma_p^2 + \sigma_n^2$. The Gaussian noise has zero kurtosis, so its addition will decrease the kurtosis of the composite, Equation (16), by the factor σ_p^4/σ_0^4 . The areal density of flux elements follows directly from the magnetogram's kurtosis, K_0 , and properties of the elements

$$n = \left(1 - \frac{\sigma_n^2}{\sigma_0^2}\right)^2 \frac{\chi}{4\pi r_*^2} \frac{\xi}{K_0} . \quad (17)$$

Having found the density, expression (15) can be used to find the root-mean-square (rms) amplitude of the flux, $\langle\phi^2\rangle^{1/2}$.

Using the above reasoning we may model a quiet sun magnetogram as a combination of Gaussian white noise and a random distribution of flux elements. The magnetogram in Figure 1b, for example, has a power spectrum which, after removal of white noise, fits an exponential $S(k) \sim e^{-2kd}$, with $d \simeq 2.2$ Mm. The magnetogram has a standard deviation $\sigma_0 = 15.8$ G, only $\sigma_n = 8.8$ G of which comes from white noise. Assuming an exponential distribution of flux amplitudes ($\xi = 6$) the kurtosis, $K_0 = 38$, implies a flux element density, $n = 0.0039 \text{ Mm}^{-2}$, from Equation (17). Equation (15) then gives the rms flux, $\langle\phi^2\rangle^{1/2} = 2.3 \times 10^{19}$ Mx. The exponential flux distribution and zero mean value can be used to convert the rms to $\langle|\phi|\rangle = 1.6 \times 10^{19}$ Mx.

Figure 14a shows a magnetogram synthesized from the distribution of sources described above. Its parameters were chosen to resemble the five-minute average low resolution magnetogram of 1b, and the two have indistinguishable power spectra (Figure 14b). The standard deviation and kurtosis of the synthetic magnetogram, $\sigma_0 = 16.1$ G and $K_0 = 39$, are well matched to the original.

Correcting the spectrum for an MTF with $\ell_0 = 1.6''$ leads to a more narrowly peaked element, $f(r)$, whose radius is $r_* = 2.1$ Mm and which has $\chi = 13.2$ (compared to $r_* = \sqrt{2}d = 3.1$ Mm and $\chi = 6.4$ without correction; see Figure 13). These more peaked elements must be distributed with greater areal density and smaller mean flux in order to match the observed kurtosis and standard deviation: $n = 0.016 \text{ Mm}^{-2}$ and $\langle|\phi|\rangle = 5.6 \times 10^{18}$ Mx. The instrument's point spread function blurs each element reducing the total apparent variance. The MTF correction thereafter amplifies the observed variance leading us to the inference of a higher density of fundamental elements. In this case by a factor of four.

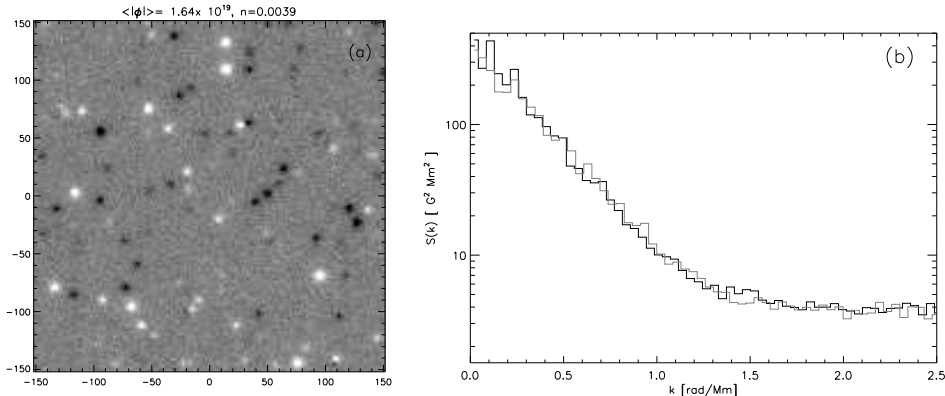


Fig. 14.— A magnetogram synthesized from a distribution of point sources at $d = 2.2$ Mm below the photosphere. (a) The magnetogram with grey scale over $|B_z| < 100$ G, exactly as for 1b. (b) The power spectra of this magnetogram (dark) and of Figure 1b (light).

The same analysis can be performed on all of the spectra analyzed in the previous section. The MTF correction implies fundamental elements with a median radius $r_* = 1.1$ Mm, too small to be observed directly in low resolution. As a consequence the median element density is quite large, $n = 0.046 \text{ Mm}^{-2}$, and median flux quite small, $\langle |\phi| \rangle = 0.22 \times 10^{19}$ Mx. These values are outside the range found by direct identification of flux elements in magnetograms (Schrijver *et al.* 1997; Parnell 2002; DeForest *et al.* 2007) since the correction for point spread function is not generally performed. Indeed, our final results depend quite sensitively on this correction, since unresolved elements contribute only slightly to the statistics of the observed magnetic field.

We repeat our analysis without the MTF correction to obtain an estimate which is at once more conservative and more consistent with previous investigation. Figure 15 shows the depth (bottom panel), areal density, n (middle panel) and flux, $\langle |\phi| \rangle$ (top panel) from low resolution magnetograms over the 2006-2007 solar minimum. These exhibit the same slow variation as the null density, presumably for the same reason: gradual variation of focus. The MTF-corrected version (not shown) has still more pronounced variation due to its amplification of the high-wavenumber portion of each spectrum. The median depth is $d = 1.43$ Mm, and without the MTF correction the median values for areal density and mean flux are $n = 0.007 \text{ Mm}^{-2}$ and $\langle |\phi| \rangle = 1.0 \times 10^{19}$ Mx respectively. These are the values for which the observations provide direct evidence and are consistent with studies which directly identify flux elements (Schrijver *et al.* 1997; Parnell 2002; DeForest *et al.* 2007).

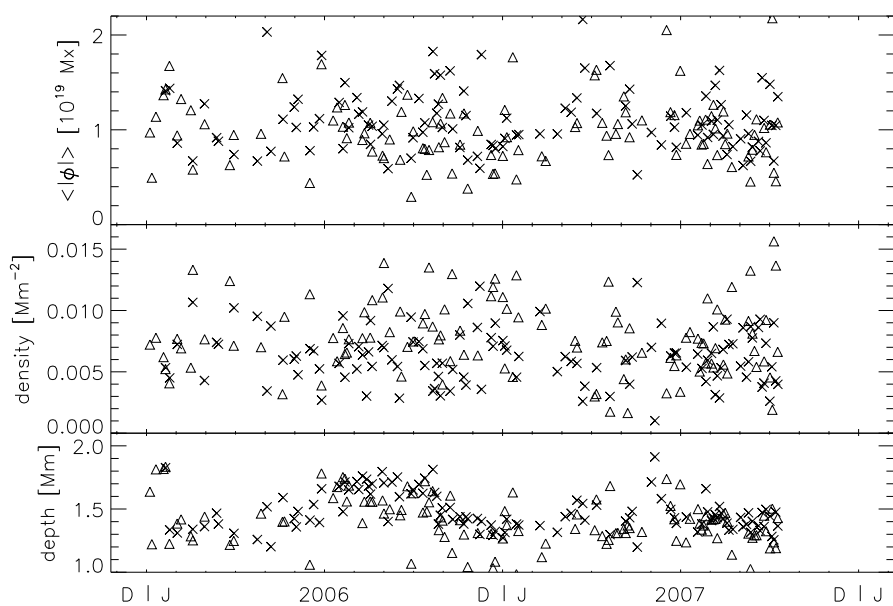


Fig. 15.— Parameters for the model magnetograms derived from spectra of one-minute (triangles) and five-minute (crosses) full-disk magnetograms. (top) The mean unsigned flux, $\langle |\phi| \rangle$, in units of 10^{19} Mx. (middle) The density of sources in units of Mm^{-2} . (bottom) The depth d at which the sources are placed.

4.2. Using the model in a noise-free spectral estimate

Submerged point sources alone, without the addition of white noise, have the same purely exponential power spectrum as the noise-corrected magnetograms. It was found in LBP03, however, that the spectral estimate grossly overestimates the column of null points above a distribution of submerged point sources. This was attributed to a severe departure from gaussianity within a layer extending $\Delta z \sim n^{-1/2}$ from the source plane ($z \leq 15$ Mm in our case). One symptom of this departure is the divergence of the kurtosis given by Equation (6). The known overestimation for point sources raises concerns about the accuracy of the spectral estimate from the noise-corrected magnetogram spectrum, which has the same spectrum.

To further explore this comparison we reduced the noise in the low-resolution 5-minute averaged magnetogram, Figure 1b, using a Fourier filter. Amplitudes of all high-spatial frequency Fourier modes ($|\mathbf{k}| > 0.7$ rad/arcsec) were rescaled to fit a pure exponential, $S(k) \propto e^{-2kd}$ with $d = 2.2$, while retaining their original phases. The result was a magnetogram (see Figure 16) which is visibly cleaner, albeit blurrier than the original (Figure 1b). The central core of its distribution function fits a Gaussian of width $\sigma_z^{(g)} = 7.0$ G. The original, 5-minute averaged magnetogram had $\sigma_z^{(g)} = 10.6$ G of which $k_c \sqrt{\pi S_n} = 8.8$ G was found to be white noise, leaving $\sigma_z = 5.9$ G to be genuine. Thus it would seem our Fourier filtering removes a substantial amount of the noise.

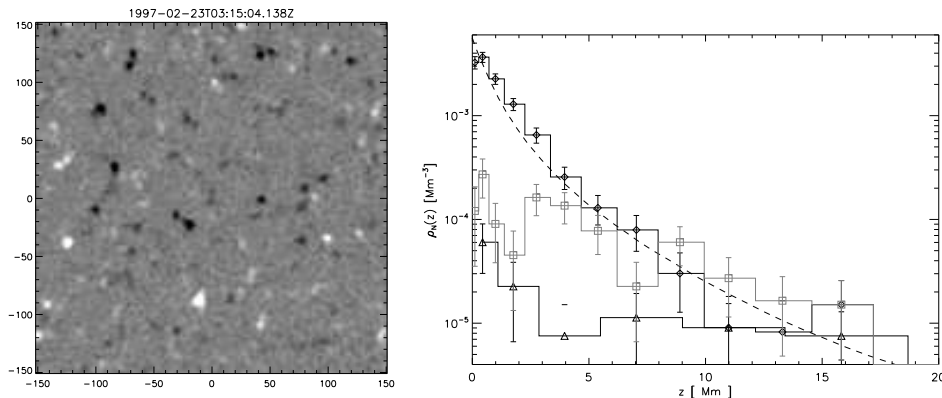


Fig. 16.— The result of Fourier filtering the low-resolution 5-minute average magnetogram Figure 1b. (left) The magnetogram plotted using the same grey scale as the original. (right) The null densities, $\rho_N(z)$, for the Fourier-filtered magnetogram (diamonds) compared to the spectral estimate (dashed). The null densities from the synthetic magnetograms created with low and high densities of submerged point sources are plotted with triangles and squares respectively.

The Fourier-filtered magnetogram has, by construction, a psd similar to a magnetogram synthesized from submerged point sources (like Figure 14a without added noise). Such a magnetogram was synthesized, extrapolated onto a grid and all its null points located using the algorithm of Haynes and Parnell (2007). The result was a column density $N_n(1.5 \text{ Mm}) = 0.3 \times 10^{-3} \text{ Mm}^{-2}$ of null points. Repeating the procedure for the Fourier filtered magnetogram yielded a column, $N_n(1.5 \text{ Mm}) = 3.6 \times 10^{-3} \text{ Mm}^{-2}$, more than an order of magnitude greater. The spectral estimates for both cases (which have similar spectra) is $N_n(1.5 \text{ Mm}) = 2.0 \times 10^{-3} \text{ Mm}^{-2}$; this is smaller than the results from the previous section, which also include MCT-correction.

The spectral estimate exceeds the column above point sources by about a factor of seven, in agreement with the finding of LBP03 (they find an actual column $N_n(-d) = 0.074n = 0.29 \times 10^{-3} \text{ Mm}^{-2}$). On the other hand, it *underestimates* the column above the filtered magnetogram by 44%, in spite of its very large kurtosis: $K_z = 49.0$ (larger than the magnetogram before filtering).

To explore the significance of kurtosis, a second synthetic magnetogram was constructed with a greater areal density ($n = 10^{-2} \text{ Mm}^{-2}$) of point sources at the same depth ($d = 2.2$) but with correspondingly smaller flux ($\langle |\phi| \rangle = 0.69 \times 10^{19} \text{ Mx}$) to endow it with the same spectrum as the other two. The kurtosis of the resulting magnetogram ($K = 29$) is lower than either of the others. A gridded extrapolation of this field was found to have a column $N_n(1.5 \text{ Mm}) = 1.0 \times 10^{-3} \text{ Mm}^{-2}$. Moreover, the actual density, $\rho_N(z)$ falls well below the spectral estimate below $z = n^{-1/2} - d = 7.8 \text{ Mm}$, as shown in the right panel of Figure 16. In contrast, the null density of the Fourier-filtered magnetogram tracks the spectral estimate, but is slightly above it, over the entire range of heights. The height at which the null density of the first synthetic magnetogram becomes accurate, is $z = n^{-1/2} - d = 13.8 \text{ Mm}$, consistent with Figure 16b.

These experiments suggest that the accuracy of the spectral estimate in predicting the actual null point column, is unaffected by the absence of white noise. For both the filtered and unfiltered 5-minute magnetogram it underestimates the column by a similar factor. This performance is far better than it would be if the photospheric field consisted of submerged point sources, as its spectrum suggests. The discrepancy cannot be explained by kurtosis of the fields, since the spectral estimate is still too large for a point-source-derived field with smaller kurtosis. It seems that the spectral estimate owes its success in the quiet Sun to a field intrinsically more complex than one from point sources.

5. Discussion

The foregoing has shown that the Fourier spectra of quiet Sun magnetograms have an invariant basic form, at least over moderately high wave numbers ($0.2 \text{ rad/arcsec} < k < 1.5 \text{ rad/arcsec}$). This spectral range plays the greatest role in dictating the distribution of magnetic null points in the corona above. As a consequence we find that the density of magnetic null points in a potential field extrapolation is about $N_n(1.5 \text{ Mm}) = 3.1 \times 10^{-3} \text{ Mm}^{-2}$ over any patch of quiet Sun, varying by roughly 10% from day to day. This value is just more than twice the number of nulls found by Régnier, Parnell and Haynes (2008) at heights greater than 1.5 Mm, using Hinode data of much higher resolution. The discrepancy could possibly arise from the much greater flux imbalance over that particular magnetogram. The column we find corresponds to 2 nulls above every 5 hexagonal, 14-Mm-diameter supergranules (Hagenaar, Schrijver and Title 1997) .

The potential magnetic field extrapolated from a photospheric magnetogram tends to become spatially smoother at increasing heights. This is a general property of harmonic functions and their gradients. One consequence is that the density of null points in such a field decreases with height and most of the null points are found close to the surface. Of the null points above $z = 1.5 \text{ Mm}$ roughly 75% are found within the next 3.0 Mm. We find the spectral estimate of the null point density in the generic quiet Sun to be $\rho_n(z) \simeq 0.04/(z + d)^{-3}$, where $d \simeq 1.4 \text{ Mm}$. This simple functional form follows from the approximately exponential nature of the photospheric spectrum.

The density at very low heights, say $z < 1 \text{ Mm}$, is dictated by very small horizontal structure in the photospheric field. This structure is the most challenging to observe, and its observation is subject to the most instrumental distortion. Moreover, this lowest atmospheric layer, the chromosphere, has the greatest plasma pressure and mass density and is least likely to satisfy the conditions which would render a magnetic field potential, or even force free. For these reasons we choose to focus our investigation on null points above $z = 1.5 \text{ Mm}$. This nominal height has nothing to do with the empirical depth, d , characterizing the exponential slope of the photospheric spectra. Rather, it arose from our experience with different instrumentation (MDI low-resolution *versus* high-resolution) and different methods of accommodating instrumental effects such as the MTF. We found that the null point density, $\rho_N(z)$, varied less above $z = 1.5 \text{ Mm}$ due to these instrumental factors, so we deemed it to be more accurately measured there.

The density and distribution of null points in the corona is predicted somewhat reliably, although not perfectly, by spectral estimate of Longcope, Brown and Priest (2003, LBP03). Magnetic null points can be found directly, and thus with more accuracy, in a potential field extrapolated from a photospheric magnetogram. We used this technique to test the

spectral estimate, and found it predicted the shape of the density, $\rho_N(z)$, reasonably well. The spectral estimate of the total column was, however, too low by a factor of two to three above one Mm. If the spectral estimate for every magnetogram is low by the same factor, then the actual null density in the quiet Sun would be greater than the value we report.

This discrepancy is most likely due to a departure of the actual field from the statistical properties assumed by the spectral estimate (homogeneity and Gaussianity). We did not find a satisfactory method of quantifying these factors. One characteristic in particular, the kurtosis of the distribution, did not accurately predict when the assumptions were adequately satisfied. We did find, however, that the conditions appear to be better satisfied, and the predictions better, for actual magnetograms than for a random distribution of point magnetic sources. In the latter case the spectral estimate *exceeds* the number of null points by at least an order of magnitude.

Although it is more accurate, direct enumeration of magnetic null points suffers from several disadvantages relative to the spectral estimate. It is more computationally expensive, so performing the search on over 500 different grids would be prohibitive. More significantly, instrumental artifacts such as noise and MTF are much more difficult to remove from the extrapolation than to remove from the spectrum. We found that white noise present in MDI magnetograms can contribute artificial null points outnumbering the real ones by as many as five-to-one. The ease with which such factors can be removed the Fourier spectra makes the spectral estimate a superior one, even given its inaccuracy.

We found that the spatial spectrum of the quiet Sun magnetic field is well approximated as an exponential, at least for $k > 0.2$ rad/Mm. This spectrum is consistent with the potential field from point magnetic sources submerged to a depth of $d \simeq 1.4$ Mm. These manifest themselves on the photosphere as circular concentrations of flux, approximately $r_* = 2.5$ Mm in radius. We are able to infer the size and areal density of these structures, $\langle |\phi| \rangle = 1.0 \times 10^{19}$ Mx and $n = 0.007$ Mm⁻², solely from the statistics of the photospheric field. The resolution of such structures into finer elements, clearly seen in high-resolution observations, will affect the spectrum only at higher wavenumbers. The spectral form we observe suggests that such fine scales are prone to cluster into 2.5 Mm concentrations.

Along similar lines, the imprint of structuring at still larger scales, such as by the network, manifests itself at lower wavenumbers, $k < 0.2$ rad/Mm. We find that actual quiet Sun spectra differ the most over these low wavenumbers, suggesting more pronounced day-to-day variation at these larger scales. Furthermore, any particular spectrum departs most from its exponential form over these low wavenumbers. This can be explained using fundamental elements distributed non-uniformly across the surface — concentrated, for example along network boundaries. This spectral range dictates the distribution of null points at great

heights, where very few ever occur. Thus the variation has virtually no effect on the total column we report.

We performed our analysis on 562 different patches ($300'' \times 300''$) of quiet Sun found at disk center over two different solar minima (1996-1998 and 2006-2007). The magnetograms were chosen to be free of active regions, plage or dominance of a single polarity. No other data was used to determine if the region was, for example, part of a coronal hole. Given their equatorial locations, however, it seems unlikely that much coronal hole data was included in our survey. We cannot therefore say whether the null point density applies to coronal holes as well as to equatorial quiet Sun.

These findings place in a clearer context observations and models with putative relationships to coronal null points. If the quiet Sun corona is being heated primarily through dissipation at null points, then the majority of this heat is supplied very low in the corona. The region between $z = 1.5$ Mm and $z = 4.5$ Mm contains three times as many nulls as the whole space above it; it would therefore probably receive a proportional share of the heating. It remains to be investigated whether the actual thermal structure of the quiet Sun corona is consistent with this distribution of heating, and is therefore consistent with heating by energy dissipation at null points.

Along similar lines, if coronal jets were hypothesized to form anywhere a coronal null point occurs, then our results can be used in an *ab initio* prediction of their frequency. Moreover, the distribution of their cusp heights should be somehow influenced by the distribution of null heights: short jets should out-number tall ones. Actual jets undoubtedly involve many factors, in addition to magnetic geometry, which influence the distribution of their properties. Still, it would be difficult to invoke null points as a requirement for jets if jets of a given height outnumbered null points at that level. A survey of coronal jets comprehensive enough to determine their frequency would thereby cast some light on the importance of null points in their construction.

A. Estimating the modulation transfer function (MTF)

To estimate the MTF, consider an ideal imaging system characterized by the same point spread function at every point on the image plane (i.e. an isoplanatic system). In this case the power spectral density (psd), $S(k)$, of the image is the product of the actual psd, $\tilde{S}(k)$, and the square of the modulation transfer function (MTF), $M(k)$ (Born and Wolf 1980). The MTF is the magnitude of the Fourier transform of the normalized point spread function. Generally, $M(k)$, is a decreasing function of wave-number, causing the observed psd, $S(k)$,

to be steeper than the actual one, $\tilde{S}(k)$.

If the same field is observed by MDI in both its high and low resolution modes the underlying psd, $\tilde{S}(k)$, will be the same for both images. In this case

$$\frac{S_{\text{lo}}(k)}{S_{\text{hi}}(k)} = \frac{M_{\text{lo}}^2(k)}{M_{\text{hi}}^2(k)} . \quad (\text{A1})$$

The MTF of the low resolution images will be dominated by the defocussing intended to reduce aliasing from spatial frequencies above the Nyquist limit $k_n = 1.6$ rad/arcsec (Scherrer *et al.* 1995). It is this contribution we can ascertain by cross comparison.

One-minute high resolution magnetograms were obtained for 11 different intervals on five different dates throughout 2007 while MDI was in focus position 5. A single psd, $S_{\text{hi}}(k)$, was constructed for each time interval. In cases where several (typically 4) consecutive one-minute magnetograms were available from a given interval, the individual psd's were averaged together to produce $S_{\text{hi}}(k)$ with lower noise. The nearest 96-minute full disk low-resolution magnetogram was then used to compute $S_{\text{lo}}(k)$. The high and low resolution magnetograms were separated by six to 30 minutes (typically 10 minutes) strengthening the assumption that $\tilde{S}(k)$ is the same for both observations.

All psd's were computed as described in section 3.1 using spectral annuli of width $\Delta k = 0.05$ rad/arcsec, and the white noise floor was subtracted from each psd. The ratio of Equation (A1) was computed over the range $k < 1.5$ rad/arcsec where both spectra were available and fairly free of noise. Full disk magnetograms have been re-calibrated by the MDI instrument team while high-resolution magnetograms have not. To compensate for the different calibration we divided the ratio by the mean of its lowest 8 spectral bins ($k < 0.4$ rad/arcsec).

A median MTF ratio is constructed by taking the median value of $S_{\text{lo}}(k)/S_{\text{hi}}(k)$ from all 11 time intervals for each spectral bin (see Figure 17a). It is fairly flat over the long-wavelength range and decays to low values by $k > 1.2$ rad/arcsec. Although the low resolution magnetograms extend out to $k_c = 1.8$ rad/arcsec, it appears there is little sensitivity over that last third of that range.

The estimated MTF ratio from Figure 17a was fitted, over the range 0.1 rad/arcsec $< k < 1$ rad/arcsec, by a variety of empirical functions. Dashed and dotted curves show two of the more successful functions

$$M_{\text{lo}}^2/M_{\text{hi}}^2 = \frac{A}{1 + \ell_0^4 k^4} , \quad (\text{A2})$$

$$M_{\text{lo}}^2/M_{\text{hi}}^2 = A' e^{-r_0^2 k^2} , \quad (\text{A3})$$

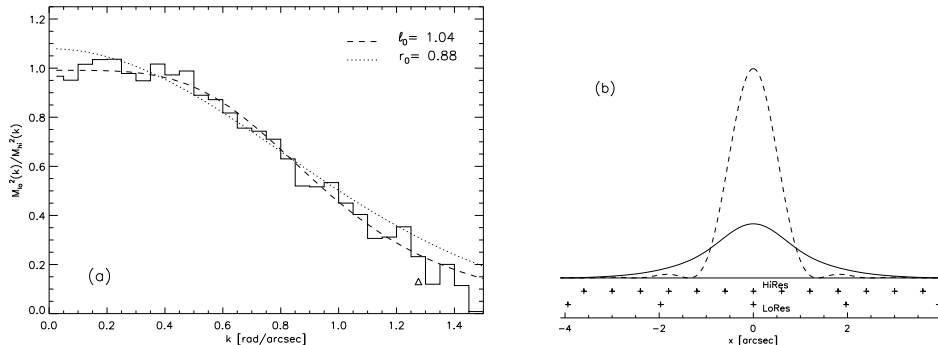


Fig. 17.— The MTF and point spread function used for MDI. (a) The median of MTF estimates from 11 quiet Sun observations. The dark solid curve is the estimate from the ratio of Equation (A1). Dashed and dotted curves are empirical fits. The triangle is the pre-launch value of the ratio quoted by Scherrer *et al.* (1995). (b) The point spread functions for the high resolution (dashed) and low resolution (solid) based on the MTF calculation. Sample pixel locations for each resolution are shown below the curves with crosses.

respectively. The best fits were for parameter values $\ell_0 = 1.04''$ and $r_0 = 0.88''$. The former curve better fits the flat inner region and the steeper fall-off beyond $k \simeq 0.6$ rad/arcsec. There is evidence that the actual MTF falls even faster, perhaps even reaching zero, for $k > 1.4$ rad/arcsec. Dividing the observed spectrum by expression (A2) is therefore a conservative correction at the very highest wave numbers.

While this cross comparison provides the ratio of the two MTFs, it cannot give any information about either one alone. The most conservative correction to either spectrum is to assume the high-resolution mode is diffraction limited and in perfect focus. In this case its MTF would be (Ghatak and Thyagarajan 1978)

$$M_{\text{hi}}(k) = M_d(k) = \frac{2}{\pi} \left[\cos^{-1} \left(\frac{k}{k_0} \right) - \frac{k}{k_0} \sqrt{1 - \frac{k^2}{k_0^2}} \right], \quad (\text{A4})$$

where $k_0 = 2\pi d/\lambda_{\text{Ni}} = 5.63$ rad/arcsec for a primary mirror of diameter, $d = 12.5$ cm and optical wavelength $\lambda_{\text{Ni}} = 6768\text{\AA}$ (Scherrer *et al.* 1995).

Scherrer *et al.* (1995) reported that the intentional defocussing reduced the low resolution MTF at $k = 0.8k_n = 1.3$ rad/arcsec to $M = 0.17$ from its diffraction-limited value of $M_d = 0.47$. That is to say $M_{\text{lo}}/M_{\text{hi}} = 0.36$, under our assumption that $M_{\text{hi}} = M_d$. The square of this value is plotted as a triangle in Figure 17. Our data point is consistent with this value, but the empirical fits are greater at this end of the spectrum. Using the empirical fits will then under-correct the highest wave-numbers.

We wish to thank Phil Scherrer, Todd Hoeksema, Jesper Schou and Craig DeForest for helpful discussions concerning MDI. This work was supported in part by NASA’s TR&T program.

REFERENCES

- Abramenko, V., Yurchyshyn, V., Wang, H., Goode, P. R.: 2001, *Solar Phys.* **201**, 225.
- Antiochos, S. K.: 1998, *Astrophys. J.* **502**, L181.
- Beveridge, C., Priest, E. R., Brown, D. S.: 2004, *Geophysical and Astrophysical Fluid Dynamics* **98**, 429.
- Born, M., Wolf, E.: 1980, *Principles of Optics: Electromagnetic theory of propagation and diffraction of light*, Pergamon Press, New York, NY, sixth edition.
- Cirtain, J. W., Golub, L., Lundquist, L., van Ballegooijen, A., Savcheva, A., Shimojo, M., DeLuca, E., Tsuneta, S., Sakao, T., Reeves, K., Weber, M., Kano, R., Narukage, N., Shibasaki, K.: 2007, *Science* **318**, 1580.
- Close, R. M., Parnell, C. E., Priest, E. R.: 2004, *Solar Phys.* **225**, 21.
- Craig, I. J. D., Fabling, R. B., Henton, S. M., Rickard, G. J.: 1995, *Astrophys. J.* **455**, L197.
- Craig, I. J. D., McClymont, A. N.: 1993, *Astrophys. J.* **405**, 207.
- Culhane, L., Harra, L. K., Baker, D., van Driel-Gesztelyi, L., Sun, J., Doschek, G. A., Brooks, D. H., Lundquist, L. L., Kamio, S., Young, P. R., Hansteen, V. H.: 2007, *Pub. Astron. Soc. Japan* **59**, 751.
- DeForest, C. E., Hagenaar, H. J., Lamb, D. A., Parnell, C. E., Welsch, B. T.: 2007, *Astrophys. J.* **666**, 576.
- Dungey, J. W.: 1958, *Cosmic Electrodynamics*, Cambridge University Press, Cambridge, U.K.
- Galsgaard, K., Nordlund, A.: 1997, *J Geophys. Res.* **102**, 231.
- Ghatak, A. J., Thyagarajan, K.: 1978, *Contemporary Optics*, Plenum Press, New York.
- Greene, J. M.: 1988, *J Geophys. Res.* **93**, 8583.
- Hagenaar, H. J., Schrijver, C. J., Title, A. M.: 1997, *Astrophys. J.* **481**, 988.

- Hassam, A. B.: 1992, *Astrophys. J* **399**, 159.
- Haynes, A. L., Parnell, C. E.: 2007, *Phys. Plasmas* **14**, 2107.
- Hesse, M., Schindler, K.: 1988, *J Geophys. Res.* **93**, 5559.
- Hufnagel, R. E., Stanley, N. R.: 1964, *J. Optical Soc. America* 52–61.
- Liu, Y., Norton, A. A.: 2001, Mdi measurement errors: The magnetic perspective, Technical Report SOI Technical Note 01-144, Standford SOI.
- Longcope, D. W., Brown, D. S., Priest, E. R.: 2003, *Phys. Plasmas* **10**, 3321.
- McLaughlin, J. A., Hood, A. W.: 2004, *Astron. Astrophys.* **420**, 1129.
- Moreno-Insertis, F., Galsgaard, K., Ugarte-Urra, I.: 2008, *Astrophys. J* **673**, L211.
- Parnell, C.: 2002, *Mon. Not. Roy. Astron. Soc.* **335**, 389.
- Pontin, D. I., Galsgaard, K.: 2007, *J Geophys. Res.* **112**, 3103.
- Press, W. H., Flannery, B. P., Teukolsky, S. A., Vetterling, W. T.: 1986, *Numerical Recipes: The art of scientific computing*, Cambridge University Press, Cambridge.
- Régnier, S., Parnell, C. E., Haynes, A. L.: 2008, *Astron. Astrophys.* **484**, L47.
- Rickard, G. J., Titov, V. S.: 1996, *Astrophys. J* **472**, 840.
- Scherrer, P. H., Bogart, R. S., Bush, R. I., Hoeksema, J. T., Kosovichev, A. G., Schou, J., Rosenberg, W., Springer, L., Tarbell, T. D., Title, A., Wolfson, C. J., Zayer, I., MDI Engineering Team: 1995, *Solar Phys.* **162**, 129.
- Schrijver, C. J., Title, A. M.: 2002, *Solar Phys.* **207**, 223.
- Schrijver, C. J., Title, A. M., Hagenaar, H. J., Shine, R. A.: 1997, *Solar Phys.* **175**, 329.
- Seehafer, N.: 1986, *Solar Phys.* **105**, 223.
- Shibata, K., Ishido, Y., Acton, L. W., Strong, K. T., Hirayama, T., Uchida, Y., McAllister, A. H., Matsumoto, R., Tsuneta, S., Shimizu, T., Hara, H., Sakurai, T., Ichimoto, K., Nishino, Y., Ogawara, Y.: 1992, *Pub. Astron. Soc. Japan* **44**, L173.
- Shimojo, M., Hashimoto, S., Shibata, K., Hirayama, T., Hudson, H. S., Acton, L. W.: 1996, *Pub. Astron. Soc. Japan* **48**, 123.

Sweet, P. A.: 1958, in B. Lehnert (ed.), *Electromagnetic Phenomena in Cosmical Physics*, 123–134, Cambridge University Press, Cambridge, U.K.

Yokoyama, T., Shibata, K.: 1996, *PASJ* **48**, 353.